Electronic Supplementary Information to

Cross-conjugation and Quantum Interference: a General Correlation?

Hennie Valkenier[a], Constant M. Guédon[b], Troels Markussen,[c] Kristian S. Thygesen,[c]
Sense J. van der Molen[b], Jan C. Hummelen[a]

a) Stratingh Institute for Chemistry and Zernike Institute for Advanced Materials, University of Groningen, Nijenborgh 4, 9747 AG Groningen, The Netherlands

b) Kamerlingh Onnes Laboratorium, Leiden University, Niels Bohrweg 2, 2333 CA Leiden, The Netherlands

c) Department of Physics, Center for Atomic-scale Materials Design, Technical University of Denmark, DK-2800 Kgs. Lyngby, Denmark

Contents

Experimental Details on Synthesis and Characterization of the Compounds

General

All reactions were performed under a nitrogen atmosphere, using dry solvents and oven dried glassware (150 °C). Chemicals were purchased from Aldrich, Acros, or Alfa-Aesar and used as received, unless stated otherwise. Tetrahydrofuran (THF) was dried by percolation over columns of aluminium oxide and R3-11 supported Cu-based oxygen scavengers. Triethylamine was distilled over KOH. Copper iodide was heated and dried under vacuum and then stored under a nitrogen atmosphere.

^{1}H and ^{13}C NMR spectra were recorded on a Varian AMX400 (400 MHz) or a Varian unity plus (500 MHz) at room temperature. Spectra were referenced to the solvent line (H, 7.26 ppm; C, 77.0 ppm). FT-IR spectra were recorded on a Nicolet Nexus FT-IR spectrometer, using the SMART iTR for ATR measurements (diamond) or in KBr using a Smart Collector DRIFT setup. Mass spectra were recorded on a Thermo Scientific Orbitrap XL or on a Jeol JMS-600H.

UV-Vis absorption spectra of the 10^{-5} M solutions in dichloromethane were measured on a Perkin Elmer Lambda 900 Spectrometer in a 1 cm quartz cuvette. The optical HOMO-LUMO gap was obtained from the onset of the absorption spectra, as found from the tangent to the inflection point.

2,6-Bis[(4-acetylthiophenyl)ethynyl]-9,10-anthraquinone (AQ-A)

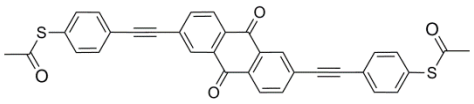

Chloroform (18 mL) was added to **AQ-B**[1] (102 mg, 0.17 mmol) and heated for a moment to obtain a yellow solution, to which acetyl chloride (5.5 mL) was added. A solution of bromine (0.2-0.5 mL, 0.3 M) in acetyl chloride/acetic acid (1:1) was added dropwise in the dark. The reaction mixture was stirred for 2-4 hours and poured into 250 mL ice water and stirred for 1 hour. The mixture was extracted with CH_2Cl_2 (3 x 200 mL), dried over Na_2SO_4, filtered, and concentrated. This reaction was repeated 3 times. The combined yellow solids (0.30 g) were preadsorbed onto silica and purified by column chromatography (silica gel, CH_2Cl_2) to yield 181 mg (0.324 mmol, 46%) of the title compound as a yellow solid.

^{1}H NMR (500 MHz, $CDCl_3$): δ 8.45 (d, J = 1.2, 2H), 8.33 (d, J = 8.0, 2H), 7.92 (dd, J = 8.0, 1.7, 2H), 7.62 (d, J = 8.3, 4H), 7.45 (d, J = 8.3, 4H), 2.46 (s, 6H). ^{13}C NMR (125 MHz, $CHCl_3$): δ 193.16, 181.87, 136.63, 134.31, 133.50, 132.42, 132.35, 130.41, 129.45, 129.27, 127.54, 123.37, 93.60, 89.45, 30.36. IR (cm^{-1}): 3065, 2923, 2219, 1702, 1670, 1589, 1324, 1303, 1276, 1245, 1121, 1101, 1090, 981, 957, 919, 881, 863, 827, 741, 711. HRMS (APCI) calculated for $[M+H]^+$ 557.0876, found 557.0834. Calcd for $C_{34}H_{20}O_4S_2$: C, 73.36; H, 3.62; S, 11.52. Found: C, 72.96; H, 3.72; S, 11.32.

2,6-Bis[(4-acetylthiophenyl)ethynyl]-9,10-dihydroanthracene (AH-H)

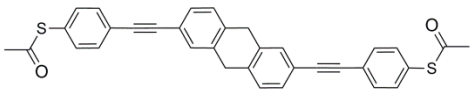

AH-B (188 mg, 0.334 mmol) was dissolved in chloroform (21 mL) and toluene (20 mL) and acetyl chloride (4 mL) was added. While stirring, BBr_3 (1 M in CH_2Cl_2, 8 mL, 8 mmol) was added slowly. The reaction mixture was stirred for 5 hours and poured into ice water (400 mL). This was extracted with CH_2Cl_2 (4 x 125 mL), dried over Na_2SO_4, filtered, and all volatiles were removed by rotary evaporation. The crude material was preadsorbed onto SiO_2 and purified by column chromatography (silica gel, CH_2Cl_2/heptane 2:1) yielding 83 mg (0.157 mmol, 47%) of the title compound as a light yellow solid.

^{1}H NMR (400 MHz, $CDCl_3$): δ 7.55 (d, J = 8.1, 4H), 7.49 (s, 2H), 7.43-7.37 (m, 6H), 7.29 (d, J = 7.8, 2H), 3.96 (s, 4H), 2.44 (d, J = 1.0, 6H). ^{13}C NMR (125 MHz, $CDCl_3$): δ 193.50, 136.93, 136.35, 134.20, 132.11, 130.57, 129.64, 127.84, 127.55, 124.66, 120.71, 91.17, 88.19, 35.82, 30.27. IR (cm^{-1}): 3057, 2926, 2859, 2209, 1705,

1498, 1415, 1396, 1124, 1109, 1100, 1089, 949, 920, 829, 811, 619. HRMS (APCI) calculated for $[M+H]^+$ 529.12905, found 529.12893. Calcd for $C_{34}H_{24}O_2S_2$: C, 77.24; H, 4.58; S, 12.13. Found: C, 77.25; H, 4.65; S, 12.03.

2,6-Bis[(4-tert-butylthiophenyl)ethynyl]-9,10-dihydroanthracene (AH-B)

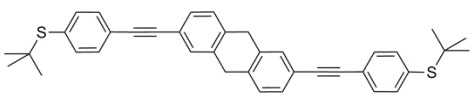

To a suspension of **3** (395 mg, 2.06 mmol), dichlorobis(triphenylphosphine)palladium(II) (147 mg , 0.21 mmol), and copper iodide (55.4 mg, 0.29 mmol) in triethylamine (35 mL) was added 1-*tert*-butylthio-4-ethynylbenzene **4** (937 mg, 4.93 mmol). The reaction mixture was refluxed for 16 hours and all volatiles were removed. The resulting solid was preadsorbed onto silica and run over a plug of silica gel, eluted with CH_2Cl_2. The product was preadsorbed onto silica and further purified by column chromatography (silica gel, CH_2Cl_2/heptane 1:2). The obtained solid was recrystallized form diethyl ether to yield 288 mg (0.52 mmol, 25%) of the title compound as a white solid.

^{1}H NMR (500 MHz, $CDCl_3$): δ 7.53-7.46 (m, *J* = 8.1, 10H), 7.39 (dd, *J* = 7.8, 1.2, 2H), 7.29 (d, *J* = 7.8, 2H), 3.96 (s, 4H), 1.30 (s, 18H). ^{13}C NMR (125 MHz, $CDCl_3$): δ 137.24, 136.84, 136.37, 133.05, 131.44, 130.52, 129.60, 127.55, 123.76, 120.87, 90.97, 88.40, 46.47, 35.85, 30.97. IR (cm^{-1}): 2960, 2919, 2894, 2859, 2209, 1500, 1417, 1361, 1169, 1152, 1014, 922, 829, 810, 803, 716. HRMS (APCI) calculated for $[M+H]^+$ 557.23312, found 557.23256. Calcd for $C_{38}H_{36}S_2$: C, 81.97; H, 6.52; S, 11.52. Found: C, 82.04; H, 6.53; S, 11.53.

2,6-Dibromo-9,10-dihydroanthacene (3)

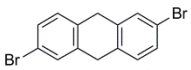

2,6-Dibromo-9,10 anthraquinone (5.27 g, 14.4 mmol), red phosphorus (4.20 g, 136 mmol) and iodine (1.00 g, 4.0 mmol) were placed in an ampule and HI (50 mL, 57% w/w in water) was added. The ampule was sealed and heated to 130-142 ºC for 3 days. After cooling an opening of the ampule, the suspension was poured into water (400 mL) and filtered. The residue was washed with cold water (200 mL) and hot water (200 mL) and dried on air. The resulting solid was dissolved in CH_2Cl_2 (400 mL), dried over Na_2SO_4, filtered, and all volatiles were removed to afford 4.1 g white solid. This was recrystallized from ethanol to yield 2.81 g (8.31 mmol, 58%) of the title compound as white needles.

^{1}H NMR (500 MHz, $CDCl_3$): δ 7.43 (d, *J* = 1.9, 2H), 7.32 (dd, *J* = 8.0, 2.0, 2H), 7.14 (d, *J* = 8.0, 2H), 3.85 (s, 4H). ^{13}C NMR (125 MHz, $CDCl_3$): δ 138.35, 134.77, 130.28, 129.25, 128.96, 119.89, 35.28. IR (cm^{-1}): 3082, 3052, 3024, 2933, 2853, 2806, 1593, 1474, 1414, 1391, 1173, 1129, 1076, 957, 913, 885, 871, 802, 724. Calcd for $C_{14}H_{14}Br_2$: C, 49.74; H, 2.98. Found: C, 48.74; H, 2.82.

Preparation and analysis of the SAMs

Dry chloroform and THF were used (Aldrich anhydrous, ≥99%). Triethylamine (Et_3N) was purchased from Fisher (HPLC grade) and degassed. All solutions and SAMs were prepared inside a glovebox filled with nitrogen (<5 ppm O_2). We used freshly prepared samples of 150 nm gold on mica for the ellipsometry and XPS studies, and freshly prepared samples of 5 nm chromium and 200 nm gold thermally deposited on a silicon wafer for the CP-AFM studies. Samples were immersed upside down for two nights in about 3 mL 0.5 mM solution in chloroform or THF, containing 10-13% triethylamine. Solutions of **AQ-A** and **AC-A** in chloroform were stirred and heated till 50°C, and filtered through a 1 µm PTFE syringe filter by gravity prior to the addition of triethylamine and monolayer growth. After the immersion time, the samples were taken from solution, rinsed three times with clean chloroform, and dried in the glovebox or with a nitrogen pistol.

Analysis of the SAMs of AC, AQ, and AH by XPS

XPS measurements were performed on a X-PROBE Surface Science Laboratories photoelectron spectrometer with a Al Kα X-ray source (1486.6 eV) and a takeoff angle of 37º. We accumulated 20 scans for S2p, 10 for C1s, 10 for O1s, 15 for N1s, and 5 for Au4f. All reported data are averaged over four different spots per sample. WinSpec[2] was used to fit the recorded data with a background and minimum number of mixed Gaussian-Lorentzian singlets (C1s, N1s, O1s) or doublets (Au4f; Δ=3.67 eV, S2p; Δ=1.18 eV) with a width of 1.21 eV.

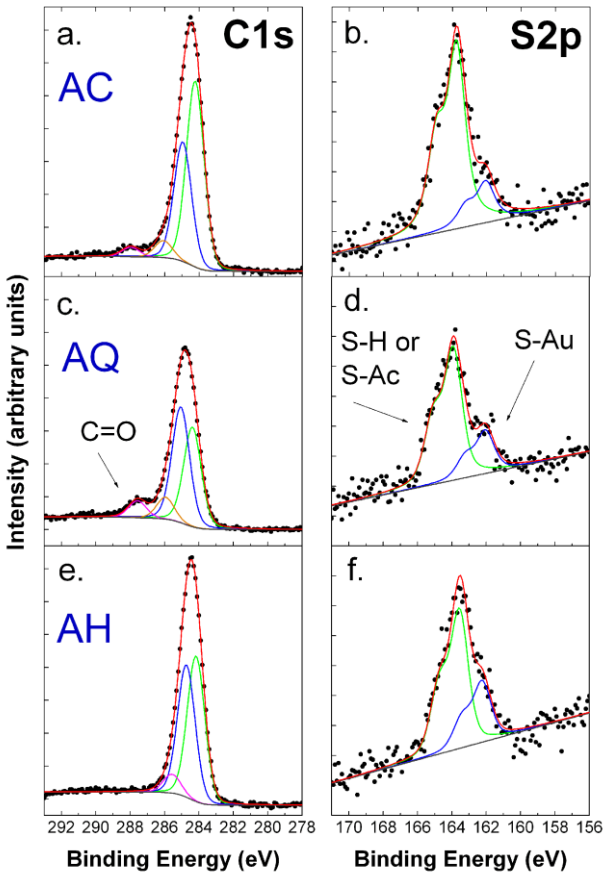

Figure S1. C1s (a, c, e) and S2p (b, d, f) XPS signals for SAMs from **AC** (a, b), **AQ** (c, d), and **AH** (e, f). Fits are shown as colored lines.

The XPS spectra of all three SAMs showed two sulfur signals (Figure S1), of which the smallest (162 eV) corresponds to sulfur bound to gold and the larger one (164 eV) to either free thiol or acetyl protected thiol. The XPS signal of sulfur bound to gold is smaller than the signal from the sulfur atoms on the top surface of the SAM, because the signal of sulfur bound to gold is attenuated by the SAM. We did not find any indication of oxidized sulfur (S=O, 168 eV). Furthermore, we found an intensity per carbon atom that approaches the average of the intensities of bound and unbound sulfur signals (Table S1). These are clear indications of a SAM comprised of molecular wires that are standing instead of lying flat on the gold surface. We found a clear C1s signal for **AQ** at 288 eV, which we attribute to the carbonyl carbon atoms of the anthraquinone core. Note that this signal has twice the intensity of a carbon atom, which agrees well with two carbonyl carbon atoms being present per molecule in the middle op de monolayer. The small carbonyl signal found for **AC** is attributed to some acetyl protecting groups being present on top of the SAM.5 We have not observed any signals from nitrogen or chlorine atoms, indicating that no solvent or base is incorporated in the SAM.

Table S1 Composition of the SAMs: X-ray Photoelectron Spectroscopy Measurements

Molecular Wire	**Integrated Intensities**[a]						**Normalized Intensities**
	Au4f	**C1s** C_xH_y	**C1s** C=O	**S2p** S-Au	**S2p** S-R	**O1s**	**C1s** per C-atom[b]
	84 eV	283-287 eV	288 eV	162 eV	164 eV	532 eV	283-287 eV
AQ	7564	1017	73	18	55	102	36
AC	7515	1343	39	19	84	57	43
AH	9919	1228	0	24	55	12	41

a. These areas are divided by the sensitivity factor: 1 for C1s, 1.79 for S2p, 2.49 for O1s, and 1.68 for N1s.

b. The total area of the C_xH_y C1s signal is divided by the number of C-atoms in the core of the molecular wire. We correct for the presence of carbonyl C-atoms.

Thicknesses of SAMs

We determined the thicknesses of the SAMs from our XPS results by two different methods: A) from the ratio between the carbon and the gold signals[3] and B) from the attenuation of the gold signals[4] (see Table 1 in the main text for the results).

Method A.[2] Thicknesses of the SAMs (d_{CS}) are determined from the ratio of the areas of C1s and Au4f peaks by equation (1) with λ_{Au} = 31 Å, λ_C = 27 Å, $d_C = d_{CS}$ - 1.8 Å (d_C is the thickness of the hydrocarbon layer without the thiolate); k is estimated to be 0.15 from XPS measurements on a SAM of undecanethiol on gold. We determined d_{CS} from I_C/I_{Au} by an iterative numerical approach.

$$\frac{I_C}{I_{Au}} = k\frac{1-\exp(-d_C/\lambda_C)}{\exp(-d_{CS}/\lambda_{Au})} \quad (1)$$

Method B.[3] Thicknesses (d) are determined from the attenuation of the Au4f signal by equation (2) with Au_0 = 109754, λ = 42 Å, and θ = 37°.

$$I_{Au} = I_{Au0}\exp(-d/\lambda\sin\theta) \quad (2)$$

In our study of SAMs of OPEs[5] we found method A to be more reliable compared to method B, since method B is more sensitive to experimental errors as alignment of the sample and intensity of the X-ray beam. However, the equation that we used to determine the thickness by method A has been derived for hydrocarbon compounds and does not take into account heteroatoms as oxygen and sulfur. The error caused by not considering unbound sulfur in method A is the same in all four SAMs. The thickness of the SAM of **AQ** is further underestimated, because of the oxygen atoms at the anthraquinone core, which can explain the relatively low value that we found for the thickness of **AQ** by method A, whereas the thicknesses of **AQ** is nearly identical to the thickness of **AC** when we use method B. We have averaged the values obtained by both methods, excluding the value obtained from the carbon/gold ratio of **AQ**, because of the presence of the oxygen atoms in this SAM.

We have also studied the SAMs by ellipsometry. These measurements were performed using a V-Vase from J. A. Woollam Co., Inc. in air. Data were acquired from 300-800 nm with an interval of 10 nm at 65, 70, and 75º angle of incidence. For every set of experiments a fresh gold-on-mica sample was measured at three or four different spots. The data from these measurements were merged and the optical constants were fitted. For every SAM three spots were measured and the thickness of a cauchy layer (n=1.55, k=0 at all λ) on top of the gold layer was fitted and averaged over the three spots. While fitting the results of these ellipsometry measurements, we assumed that the index of refraction (n) is 1.55 for all conjugated thiols and that the SAMs do not absorb between 300-800 nm (as we did for our previous study on SAMs of OPE molecules).[4] These assumptions might introduce an error in the measurements, especially for **AC**, which has strong optical transitions around 400 nm (see below). For **AQ** and **AH** we have averaged the thicknesses from the XPS and ellipsometry measurements, whereas for **AC** we only use the (average) thickness from XPS. The SAMs of cross-conjugated **AQ** and linearly conjugated **AC** thus have similar thicknesses (24 and 25 Å), whereas the SAM of **AH** is slightly thinner (19 Å)), which could be caused by the flexibility of this wire, due to the sp^3 hybridized carbon atoms introduced in the backbone on the wire.

Table S2 Thicknesses of the Self-Assembled Monolayers as determined by ellipsometry and XPS.

Molecular Wire	**Length Molecule[a] (Å)**	**Thickness SAM by Ellipsometry (Å)**	**Thickness SAM by XPS method A[2] (Å)**	**Thickness SAM by XPS method B[3] (Å)**	**Weighed Average[b] (Å)**
AQ	24.49	21.7 (3)	20.1 (0)	26.9 (3)	25
AC	24.49	28.6 (0)	24.1 (2)	27.1 (1)	24
AH	24.55	19.1 (3)	18.3 (2)	20.1 (1)	19
OPE3	20.14	19.7 (3)	17.5 (2)	17.8 (1)	19

a. The distance from sulfur to sulfur atom as obtained from DFT calculations.

b. The weights are shown in brackets. The absolute values obtained from XPS by method A are considered more accurate than those obtained by method B and therefore weighed twice as strong. Identical weights were used for ellipsometry and XPS (methods A and B combined).

Experimental Details on CP-AFM Measurements

The measurements are performed on a Multimode atomic force microscope base using a nanoscope III controller. The AFM cantilevers (Veeco NP-10 chips, B cantilever, 0.12 N/m and 14 – 26 kHz)) are sputtered with MoGe (4 nm) as an attachment layer prior to the Au layer (80 nm). Before every measurement the tips are cleaned by oxygen plasma. The samples are prepared on Au coated Si/SiO_2 substrates as described above. Subsequently, the sample is electronically connected to the scanner and the scanner is connected to the data acquisition card via the AFM breakout box. Using a modified tip holder, the cantilever is connected to the I/V converter (Femto DLPCA-200).

The AFM is operated in contact mode with the scanning range set to 0 nm in order to contact continuously the same area of the SAM. To insure a soft contact with the molecules, a force of approximately 2 nN is applied and maintained constantly using feed-back on the deflection of the cantilever.

Once the molecules are contacted, the current sensing can be switched on as it is externally driven by Labview. A bias voltage is applied to the tip-sample junction and simultaneously the current is recorded at a sampling rate of 10 kHz. We record 200 to 1000 of such I(V) curves for each of the 3 to 6 spots on each sample. The conductance histograms are built up from low bias (100 mV) conductance values from individual I(V) curves. Those conductance values are logarithmically binned and plotted linearly.

Details on Transport Calculations

The conductance is calculated using DFT in combination with a non-equilibrium Green function (NEGF) method as described in the literature[6] Our DFT-NEGF method is implemented in GPAW, which is an electronic structure code based on the projector augmented wave method supporting various types of basis sets including real space grids, plane waves and numerical atomic orbitals (used here).[6] We use the Perdew-Burke-Ernzerhof (PBE) exchange-correlation functional[7] and a 4x4 *k*-point sampling in the surface plane. The electronic wave functions are expanded in an atomic orbital basis.[8] All atoms are described by a double-zeta plus polarization (dzp) basis set. The density has been represented on a real space grid with a grid spacing of 0.2 Å.
We initially relax the molecule and the two closest Au layers until the forces on the atoms are less than 0.05 eV/Å. In the relaxed configuration, the S-atoms bind to Au at a bridge site slightly shifted toward the hollow site.

The low-bias conductance can be obtained from the Landauer formula, $G = \frac{2e^2}{h}T(E_F)$, where E_F is the Fermi energy and T is the zero-bias transmission function. Following the standard DFT-Landauer approach, we calculate the transmission function as

$$T(E) = Tr[G^r(E)\Gamma_L(E)G^a(E)\Gamma_R(E)] \quad (3)$$

with $G^r(E) = (E \cdot S - H - \Sigma_L - \Sigma_R - \Sigma_{SO})^{-1}$ being the retarded Green's function for the junction (scattering region) described by the single-particle Hamiltonian H and overlap matrix S, and where the semi-infinite electrodes are included through left and right electrode self-energies,$\Sigma_{L,R}$. The coupling matrices in (3) are related to the electrode self-energies as $\Gamma_{L,R} = -2Im(\Sigma_{L,R})$. The additional self-energy term Σ_{SO}in (3) works as a "scissors operator" which shifts the occupied states down in energy and the unoccupied states up in energy. This is included to correct for the wrong description of molecular energy levels in DFT and for image charge effects not included

in standard DFT at all. The Σ_{SO} works independently on the occupied and unoccupied molecular orbitals. The energy shift of the occupied states consists of two terms: (i) A correction Δ_0 to shift the Kohn-Sham HOMO level of the *free* molecule down in energy to match the ionization potential (IP) obtained from total energy differences between the neutral and positively charged (+1e) molecule. (ii) An upward shift Δ_q due to image charge corrections.[9,10] The unoccupied states are correspondingly shifted up in energy to correct the Kohn-Sham LUMO to coincide with the electron affinity (EA) and a (smaller) downward shift due to image charge corrections. The transmission functions calculated with pure DFT and with DFT+Σ share the same qualitative feature, but with the occupied/unoccupied states shifted down/up in energy in the DFT+Σ calculations as compared with pure DFT. The DFT+Σ method has previously been shown to yield better agreement with experimental results compared to pure DFT. [11,9] However, the exact positions of peaks and dips in the transmission function might still differ from experimental results due to uncertainties in exact binding geometry, SAM density, and the relatively simple calculation method with the rather crude scissors operator correction.

Figure S2 shows the transmission functions for **AQ**, **AC**, and **AH**. Similarly to the DFT+Σ calculated transmissions shown in the main text the **AQ** has a QI transmission dip between the HOMO and LUMO level, while the QI feature of **AH** is below the degenerate HOMO/HOMO-1 levels. In agreement with the AFM conductance measurements **AQ** has the lowest conductance (transmission at the Fermi energy, E_F) and **AC** the

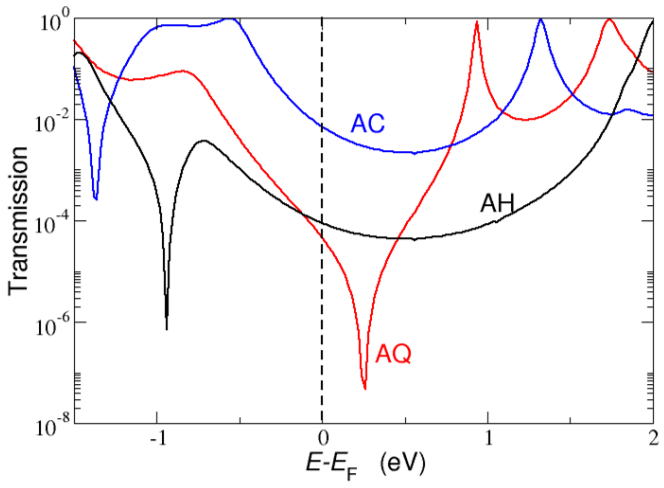

Figure S2. DFT transmission functions for **AQ** (red), **AC** (blue) and **AH** (black).
highest conductance.

Energy Differences between the HOMO and LUMO

In Table S3 we compare the experimentally observed optical gaps with three different theoretical values. The gas phase ionization potential (*IP*) and electron affinity (*EA*) are calculated with density functional theory (DFT) from total energy differences $IP = E(+e) - E(0)$, $EA = E(0) - E(-e)$, where $E(q)$ is the total energy of the neutral molecule ($q = 0$) and positively/negatively charged ($q = \pm 1e$) molecule. The gas-phase HOMO-LUMO gap is calculated as $\Delta E_{HL} = IP - EA$. The energy difference between the calculated ΔE_{HL} and the experimental optical gap is expected to be dominated by Coulombic effects, *i.e.* 'electron-hole' Coulomb attraction in the excited state, which is not present in the reduced and oxidized states. In addition, solvent effects play a role.

Table S3 Calculated HOMO-LUMO gap obtained from total energy differences (ΔE_{HL}), from Kohn-Sham energy differences ($\Delta\varepsilon_{HL}$), and from TDDFT (ΔE_{TDDFT}). The experimental values are obtained from the UV-Vis spectra.

Molecular Wire	ΔE_{HL} **(eV)**	$\Delta\varepsilon_{HL}$ **(eV)**	ΔE_{TDDFT} **(eV)**	**Experimental optical gap (eV)**
AQ	4.23	1.58	1.79	2.88
AC	4.61	1.79	2.23	2.90
AH	5.04	2.65	2.75	3.75

We also list in Table S3 the energy differences between the Kohn-Sham HOMO and LUMO energy levels. As always in DFT with semi-local functionals the Kohn-Sham energy gap is significantly smaller than the values obtained from total energy calculations.[12] Finally, we show excitation values obtained from time-dependent DFT (TDDFT) within the adiabadic local density approximation (ALDA). TDDFT should in principle yield exact optical excitation energies. However, while the commonly used ALDA approximation yield excellent results for small molecules, it is known to systematically underestimate excitation energies in larger conjugated molecules as well as solids.[13] Thus we ascribe the underestimation of 0.67 eV for **AC** to this effect. The tendency of ALDA to underestimate optical gaps has been shown to be even more severe for excitations with strong charge-transfer character[14],[15] which explains the slightly larger deviation (around 1 eV) found for the **AH** and **AQ** molecules. While the absolute numbers of all the calculations differ from the experimental values, the trends are the same for all methods and in agreement with experiments. In particular we stress that **AQ** has the smallest gap, **AC** has a similar but larger gap, and **AH** has the largest gap. When we compare the results of the optical measurements and calculated HOMO-LUMO gaps with the conductance measurements, it is striking that **AQ** and **AC** have nearly identical HOMO-LUMO gaps and lengths, but conductance values that differ about two orders of magnitude.

Localized Molecular Orbital Analysis of the Dihydroanthracene-wire

As previously shown[16] the QI effect in **AQ** can be qualitatively understood by transforming the degenerate HOMO-1 and HOMO together with the LUMO orbitals (see Figure S3) into localized molecular orbitals (LMOs). For **AC** only the HOMO and LUMO are relevant for the conductance.

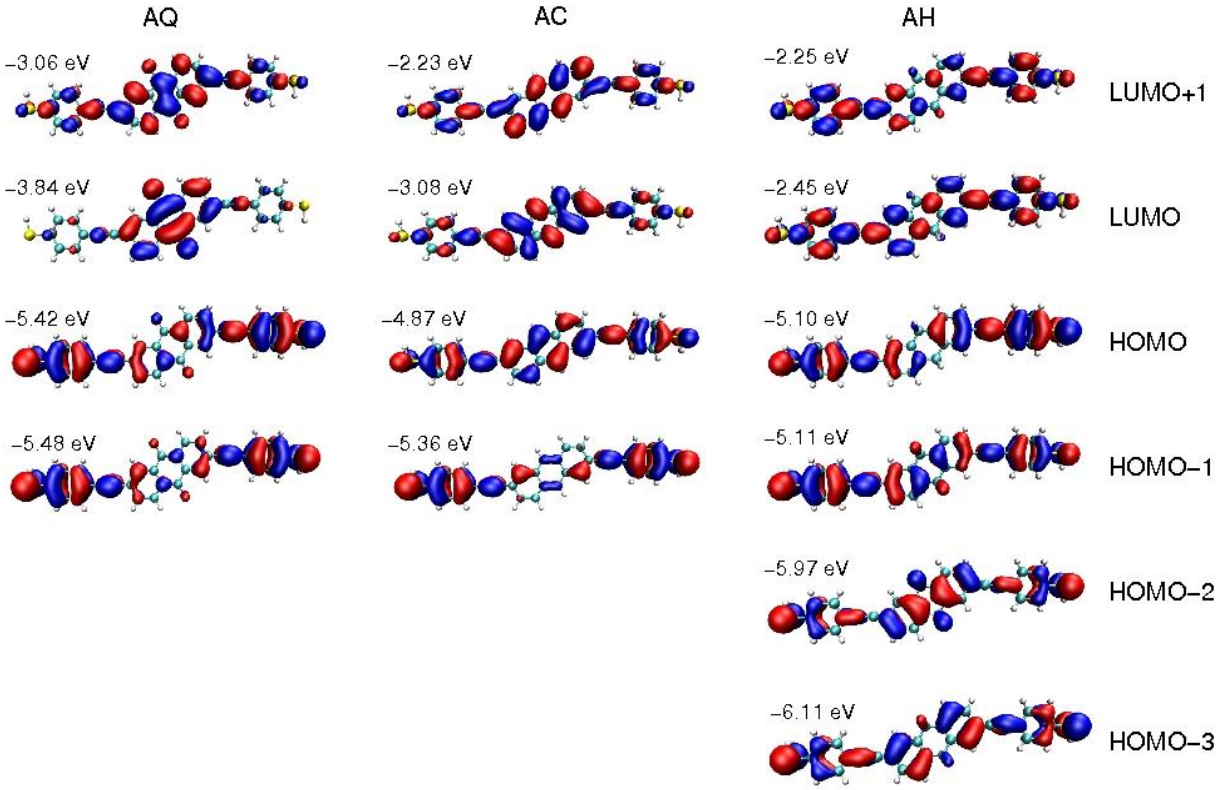

Figure S3. Molecular orbitals (MOs) of free **AQ**, **AC**, and **AH**. The Kohn-Sham orbital energies for each MO is given relative to the vacuum level.

In order to understand the transport properties of the **AH** we perform in Figure S4 a similar LMO analysis. Initially we consider only the almost degenerate HOMO and HOMO-1 orbitals – see Figure S3. The corresponding LMOs (obtained as plus and minus combinations of the HOMO and HOMO-1) are shown in Figure S4 (d). The corresponding tight-binding model is shown in panel (g) with just two sites: one coupled to the left electrode and the other coupled to the right electrode. Since there is only one path through the molecule, no QI is observed. The full transmission function [dotted line in panel (a)] is well described by the two-site model [red line in (a)] at energies around the HOMO energy. The hopping matrix element between the left and right LMOs is given by the energy difference of the HOMO and HOMO-1, $\alpha = (\varepsilon_H - \varepsilon_{H-1})/2$. Since the HOMO and HOMO-1 are almost degenerate, α is very small and the transmission around the HOMO/HOMO-1 is low with a peak value of $4 \cdot 10^{-3}$.

Including also the HOMO-2 and HOMO-3 states leads to LMOs shown in panel (e) with the corresponding TB model shown in (h). This LMO model fits the full calculation in the energy range from the HOMO-3 to HOMO including the destructive QI effect. This illustrates that the QI for the AH is due to interference between different paths involving the HOMO-3 to HOMO. Finally, considering the HOMO-1, HOMO, LUMO, and LUMO+1 leads to the LMOs in panel (f) and TB model in panel (i). Not surprisingly, panel (c) shows that this subset of MOs reproduces the full transmission function in the HOMO-LUMO gap.

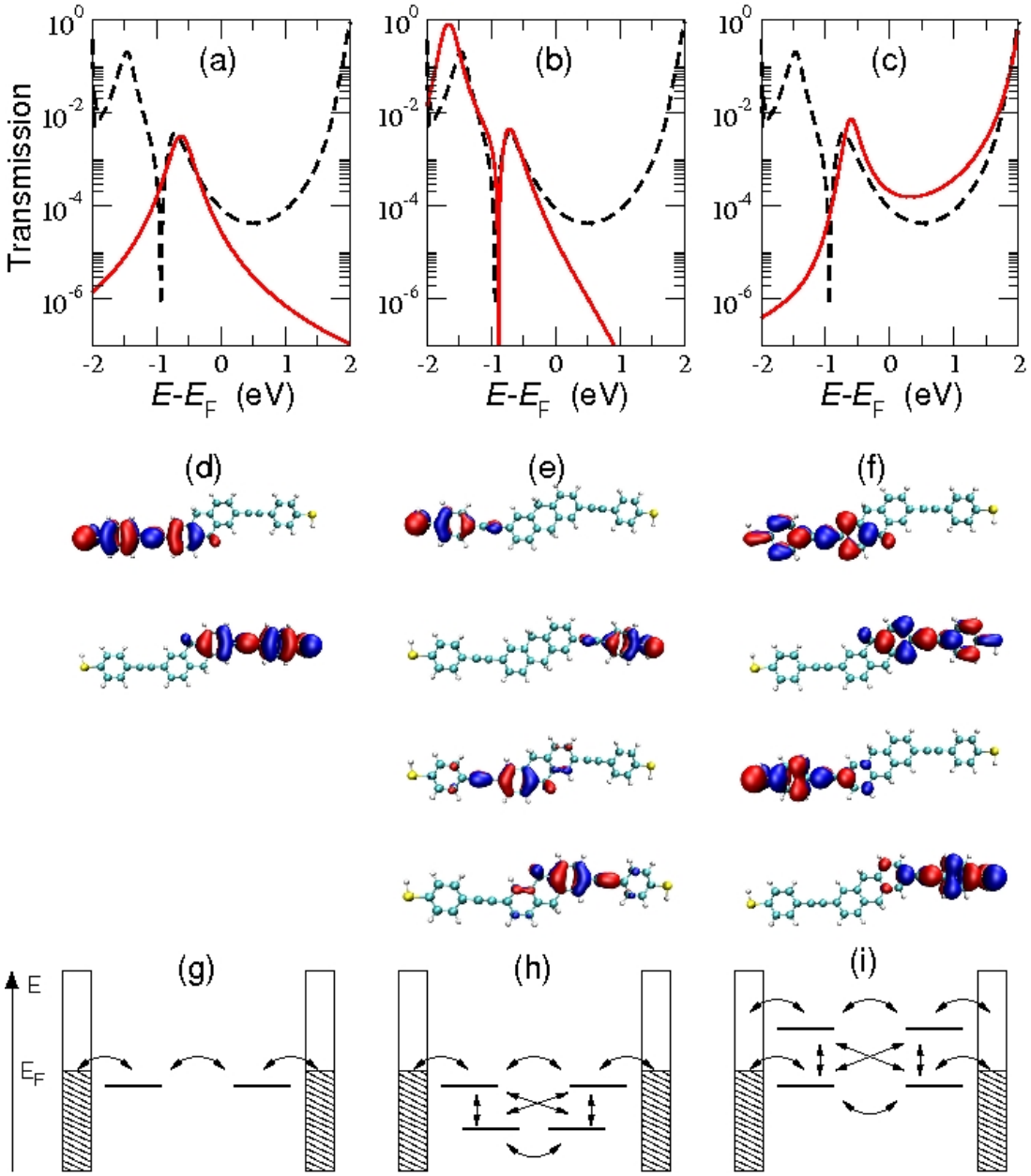

Figure S4 The full DFT-NEGF transmission function (dashed black lines in upper panels a,b,c) can be locally described with few-site TB models (red lines). The TB models shown in the bottom row (panels g,h,i) are obtained from localized molecular orbitals (LMOs) show in the middle part. The left column (panels a,d,g) only considers the HOMO and HOMO-1 which are almost degenerate (see Figure S3). The TB model transmission (red line in panel a) locally reproduces the full transmission function. In the middle column (panels b,e,h) the HOMO-3 and HOMO-2 are also included together with the HOMO and HOMO-1. The QI transmission node around E-E_F=-1 eV is clearly reproduced with the four-site TB model. In the rightmost column (panels (b,f,i) we consider the HOMO-1, HOMO, LUMO, and LUMO+1. This model reproduces the full transmission function in the HOMO-LUMO gap.

From the LMO analysis we conclude that (i) the destructive QI effect around E-E_F = -1 eV is due to an interplay of the HOMO-3 to HOMO states, and (ii) the low transmission value at the Fermi energy is caused by the degeneracy of the HOMO and HOMO-1 together with the large HOMO-LUMO gap.

This QI effect seen for **AH** can also be interpreted from the perspective of hyperconjugation, by considering the pair of two hydrogen atoms attached to the central carbon atoms as a single side group. While all other hydrogen atoms are located in the molecular plane and hence do not couple to the carbon p_z orbitals, the hydrogen atoms in the CH_2- group are not located in the molecular plane. Viewed as an isolated system, the two hydrogen atoms in the CH_2- group form a bonding orbital (symmetric in the molecular plane) and an anti-bonding orbital (anti-symmetric in the molecular plane). The bonding state will have vanishing coupling to the carbon p_z orbitals due to symmetry but the anti-bonding state will have a finite coupling (see Figure S5). Hence the dihydro anti-bonding orbital is analogous to the p_z orbital on the oxygen atoms in the **AQ** and the topology of the π systems of **AQ** and **AH** are thus very similar. It is therefore expected that both **AQ** and **AH** should display QI effects within the HOMO-LUMO gap.[17]

Figure S5 Schematic representation of the coupling between the s orbitals from the CH_2 group in **AH** and the p_z orbitals in the phenyl rings, that resembles the coupling of p_z orbitals in cross-conjugated structures.

References

[1] E. H. van Dijk, D. J. T. Myles, M. H. van der Veen, J. C. Hummelen, *Org. Lett.,* 2006, **8**, 2333-2336.

[2] WinSpec 2.09, developed at Laboratoire Interdépartemental de Spectroscopie Electronique, Namur, Belgium.

[3] J. Thome, M. Himmelhaus, M. Zharnikov, M. Grunze, *Langmuir,* 1998, **14**, 7435-7449.

[4] C. D. Bain, G. M. Whitesides, *J. Phys. Chem.,* 1989, **93**, 1670-1673.

[5] H. Valkenier, E. H. Huisman, P. A. van Hal, D. M. de Leeuw, R. C. Chiechi, J. C. Hummelen, *J. Am. Chem. Soc.,* 2011, **133**, 4930-4939.

[6] J. Enkovaara, *et al*., *J. Phys. Condens. Matter,* 2010, **22**, 253202.

[7] J. P Perdew, K. Burke, M. Ernzerhof, *Phys. Rev. Lett.,* 1996, **77**, 3865.

[8] A. H. Larsen, M. Vanin, J. J. Mortensen, K. S. Thygesen, K. W. Jacobsen, *Phys. Rev. B,* 2009, **80**, 195112.

[9] D. J. Mowbray, G. Jones, K. S. Thygesen, *J. Chem. Phys.,* 2008, **128**, 111103.

[10] J. B. Neaton, M. S. Hybertsen, S. G. Louie, *Phys. Rev. Lett.,* 2006, **97**, 216405.

[11] S. Y. Quek, H. J. Choi, S. G. Louie, J. B. Neaton, *Nano Lett.,* 2009, **9**, 3949.

[12] C. Rostgaard, K. W. Jacobsen, K. S. Thygesen, *Phys. Rev. B,* 2010, **81**, 085103.

[13] *Time-Dependent Density Functional Theory*, ed. M. A. L. Marques, C. Ullrich, F. Nogueira, A. Rubio, K. Burke, E. K. U. Gross, Springer, Berlin, 2006.

[14] A. Dreuw, J. L. Weisman, M. Head-Gordon, *J. Chem. Phys.,* 2003, **119**, 2943-2946.

[15] J. M. Garcia-Lastra, K. S. Thygesen, *Phys. Rev. Lett.,* 2011, **106**, 187402.

[16] T. Markussen, J. Schiötz, K. S. Thygesen, *J. Chem. Phys.,* 2010, **132**, 224104.

[17] T. Markussen, R. Stadler, K. S. Thygesen, *Phys. Chem. Chem. Phys*., 2011, **13**, 14311.